PCCP

ROYAL SOCIETY
OF CHEMISTRY

PAPER

View Article Online
View Journal

Check for updates

Cite this: DOI: 10.1039/d6cp00572a

Determining the molecular structures of cytochrome P450 and its complex associated with model cell membranes

Guangyao Wu,†[a] Wen Guo,†[a] Pei Yang,†[a] Rui Huang,‡[a]
Ayyalusamy Ramamoorthy[abcd] and Zhan Chen *[ab]

The lipid membrane assisted interaction between cytochrome P450 (CYP450) and its reductase (CPR) plays a significant role in many biochemical reactions and in drug metabolism. Previous solution and solid-state studies have shown the importance of the lipid bilayer in the structural folding of CYP450 and the electrostatic interactions between the soluble domains and the hydrophobic interactions between the transmembrane helical domains of CYP450 and CPR using bicelles and nanodiscs. In this study we report an effective way to determine both the conformation and the orientation of the truncated microsomal CYP450 2B4 associated with lipid membranes, and its orientation transition when binding to a truncated flavin mononucleotide binding domain of CPR. The developed methodology combines measurements using sum frequency generation vibrational spectroscopy and attenuated total reflectance–Fourier transform infrared spectroscopy, and computational data interpretation, which is powerful and generally applicable to reveal the interfacial structures of protein complexes in physiologically relevant environments.

Received 15th February 2026,
Accepted 16th March 2026

DOI: 10.1039/d6cp00572a

rsc.li/pccp

Introduction

Cytochromes P450 (CYP450), a superfamily of heme-containing enzymes, are responsible for the metabolism of steroids, xenobiotics, fatty acids and drugs. They play crucial roles in biosynthesis and bio-breakdown.[1–3] The catalytic function of CYP450 involves a two-step electron transfer process during the interaction with its redox partners F and cytochrome-b_5 (cyt-b_5).[1–5] CYP450 receives the first electron transferred from CPR and sequentially receives the second electron either from CPR or cyt-b_5, while studies have reported the role of cyt-b_5 to be substrate dependent.[1–4,6–8] Thus, knowledge about the dynamic structural interactions between CYP450 and CPR (or cyt-b_5) would give insights into the catalytic efficiency of CYP450. Previous studies found that the binding happens at the proximal face of CYP450 and the flavin mononucleotide (FMN) binding domain (FBD) of CPR.[2,9,10] The truncated-FBD (lacking the transmembrane domain (TM domain)) and truncated-CYP450 (also lacking the TM domain) are superimposed on the FBD domain in a full-length FBD (with TM domain) and CYP450 segment in a full-length CYP450 (with TM domain), respectively.[5] Therefore, the above truncated proteins can be chosen to investigate the protein–protein interactions *in vitro* for simplicity. Extensive studies have been focused on the CYP450–CPR complex associated with the lipid membrane, since the presence of lipids has been found to be an essential factor to stabilize the structural folding of CYP450 and to facilitate the accessibility of hydrophobic ligands to the active site of CYP450.[1,11–15] However, direct examination of the interfacial structures of the protein complex associated with lipid membranes *in situ* is challenging and therefore there is considerable interest in the development of new approaches.[16–20]

Sample preparation methods, such as site-directed mutagenesis,[21] and analytical techniques, such as X-ray crystallography[21,22] and nuclear magnetic resonance (NMR) spectroscopy,[1,12] are the most commonly used techniques to investigate the structure of the CYP450–CPR complex. Although these techniques have provided significant insights into the structural and functional properties of the CYP450–CPR complex with atomistic resolution,[23] there are still some limitations. For example, experimental sample conditions required

---

[a] *Department of Chemistry, 930 North University Avenue, University of Michigan, Ann Arbor, Michigan 48109, USA. E-mail: zhanc@umich.edu*

[b] *Biophysics Program, 930 North University Avenue, University of Michigan, Ann Arbor, Michigan 48109, USA*

[c] *Department of Chemical and Biomedical Engineering, FAMU-FSU College of Engineering, Florida State University, Tallahassee, FL 32310, USA*

[d] *National High Magnetic Field Laboratory, Florida State University, Tallahassee, FL 32310, USA*

† These authors contributed equally.

‡ Current address: Department of Chemistry, University of Guelph, Guelph, Ontario, N1G 2W1, Canada.

for these studies (*e.g.*, protein crystals or high concentration protein solutions) need not resemble the working conditions of the target proteins. Computational approaches, such as molecular dynamics (MD) simulations, have been applied to study the CYP450–CPR complex as well.[9] However, more direct experimental observations are needed to validate these *in silico* modeling results and explore further valuable insights. A systematic approach recently developed for interfacial protein structural study combines vibrational spectroscopies for experimental measurements, computer simulations, and Hamiltonian spectra calculations,[24–27] and is a promising and powerful strategy to reveal the interfacial structure of the CYP450–CPR complex and its interaction with the lipid membrane *in situ* by overcoming the abovementioned limitations.

For this methodology, sum frequency generation (SFG) vibrational spectroscopy, a surface-sensitive second-order nonlinear optical spectroscopy,[27–65] and attenuated total reflectance–Fourier transform infrared (ATR-FTIR) spectroscopy were applied to collect vibrational spectra of the interfacial proteins of interest. In parallel, *in silico* modeling was conducted to predict interfacial structures of the proteins. To correlate the results from experimental and computational observations, a Hamiltonian approach was then used to calculate SFG and FTIR spectra based on the predicted structures as a function of protein orientation and score the orientation-dependent calculation results based on the experimentally collected spectra for each structure. Therefore, both conformations (predicted structures from *in silico* modeling) and orientations of the interfacial protein can be determined if a match (with high ranking scores) can be found with the Hamiltonian program. Moreover, incorporation of isotope-labeling into sample preparation of vibrational spectroscopic measurements (*e.g.*, traditional infrared spectroscopy and 2D IR)[66–69] gives further advantages. Isotope-labeling could separate originally overlapped vibrational signals. For example, ^{13}C isotope substitution of backbone carbonyl can shift the amide I vibrational frequency of a labeled unit by ~40 cm^{-1}.[56,66] Since the amide I vibrations are dominated by the contribution from the C=O stretching, ^{13}C/^{15}N dual isotope labeling can be expected to work similarly to ^{13}C labeling alone.[70] The ^{13}C=^{18}O dual isotope-labeling further shifts the amide I band by ~65 cm^{-1}.[56,66,71] Isotope labeling can thus provide more independently measured spectra from the same protein structure, leading to more accurately deduced structural results.[72] Uniquely, with the help of isotope labeling, SFG can more accurately determine protein structures (conformations and orientations) at interfaces.

In this study, the most likely conformations and orientations of the complex of truncated microsomal CYP450 2B4 (trunc-CYP2B4) (without the TM domain) and truncated FBD (trunc-FBD) associated with the 1-palmitoyl-2-oleoyl-*sn-glycero*-3-phosphocholine (POPC) lipid bilayer (serving as a model for the cell membrane) were determined by the developed methodology. The backbone of trunc-FBD was ^{13}C–^{15}N isotope labeled and thus its amide I vibrational signal was shifted to a lower frequency, which was separated from the amide I signal from the non-isotope-labeled trunc-CYP2B4. This experimental design enriched the spectral features for both SFG and ATR-FTIR measurements by reducing the spectral overlaps and thus improved the accuracy of further data interpretation. The conformations and orientations of trunc-CYP2B4 alone associated with two different phosphate lipid bilayers (POPC and DLPC (1,2-dilauroyl-*sn-glycero*-3-phosphocholine)) without the presence of trunc-FBD were also determined. A membrane orientation change between the trunc-FBD-bound and unbound states of trunc-CYP2B4 was observed. This study aims to use the trunc-CYP2B4/trunc-FBD system as a simplified example to develop a generally applicable methodology to explore the structure (orientation and conformation) of a protein complex at the interface. This research also demonstrated the feasibility and power of using SFG to probe protein–protein interactions at interfaces *in situ*.

Experimental methods

Sample preparation

The unisotope-labeled truncated CYP2B4 (residues 22–491) was expressed, purified and characterized as previously described.[73,74] The FMN binding domain of the rat CPR (residues 57–239) was expressed in *E. coli* C41 cells. To produce uniformly ^{13}C and ^{15}N-labeled FMN binding domains, expression was carried out in M9 minimal media (40 mM Na_2HPO_4, 20 mM KH_2PO_4, 8.5 mM NaCl, 18 mM $^{15}NH_4Cl$, 1 mM $MgSO_4$, 1 μM $CaCl_2$, 16 nM riboflavin, 0.4% (w/v) ^{13}C-glucose) and induced at A_{600} = 0.7 with 0.4 mM isopropyl β-D-1-thiogalactopyranoside. The cells were allowed to grow at a shaking speed of 140 rpm for 14 hours at 30 °C before harvesting. The harvested cells were lysed *via* treatment with lysozyme (30 mg per ml of cell suspension) for 30 min and subsequent sonication by alternating 1-min pulses for a total of 8 min. After centrifugation at 14 000 × *g* for 20 min, the supernatant was loaded onto a DEAE-Sepharose column equilibrated with loading buffer (50 mM Tris acetate, 0.1 mM EDTA, 0.2 mM DTT, 10% glycerol, 1 mM FMN, pH 6.7). The column was washed with 2 column volumes of loading buffer and 5 column volumes of washing buffer (loading buffer with additional 0.17 M NaCl and 0.3% (w/v) sodium cholate) and gradient-eluted with a total of 4 column volumes of washing buffer and eluting buffer (loading buffer with additional 0.5 M NaCl and 0.3% (w/v) sodium cholate). The purified protein exhibited a single band on the SDS-PAGE gel.[75] The concentration of the oxidized FMN binding domain was determined using extinction coefficients of 12.2 mM^{-1} cm^{-1} at 454 nm.

POPC (1-palmitoyl-2-oleoyl-*sn-glycero*-3-phosphocholine) lipids and right-angle CaF_2 prisms were purchased from Avanti Polar Lipids (Alabaster, AL) and Altos Photonics (Bozeman, MT), respectively. For SFG experiments, the Langmuir–Blodgett and Langmuir–Schaefer (LB/LS) methods were used to deposit the proximal lipid monolayer and the distal lipid monolayer onto a CaF_2 prism, respectively, to form a lipid bilayer as a model for the cell membrane. The detailed procedure of such lipid bilayer preparation against a right-angle prism was reported previously and will not be repeated here.[26,76–81] The subphase solution in contact with the distal layer of the POPC lipid bilayer is a 10.0 mM, pH = 7.4 phosphate buffered saline (PBS) contained inside a 2 ml reservoir. CYP2B4 (4 μM in PBS buffer) was first injected into this aqueous reservoir, followed by injection of ^{13}C–^{15}N isotope-labeled FBD (4 μM in PBS buffer). The SFG spectra were then collected after the protein complex–lipid bilayer interaction reached equilibrium (∼16 min). For ATR-FTIR experiments, a Nicolet 6700 spectrometer was used to collect ATR-FTIR spectra with a standard 45° ZnSe ATR cell. Lipid bilayers were deposited onto the ZnSe crystal surface using the vesicle fusion methods reported previously.[80–82] The subphase solution in contact with the lipid bilayers was replaced to D_2O-based buffer to avoid signal confusion between the O–H bending mode and the protein amide I mode and to ensure a better S/N ratio in the protein amide I band frequency region. Similar to the SFG experimental procedure, CYP2B4 was first added into the subphase reservoir, followed by injection of ^{13}C–^{15}N isotope-labeled FBD. The final concentration of the proteins matched the final concentration used in SFG experiments. The ATR-FTIR spectra were then collected after the protein complex–lipid bilayer interaction reached equilibrium (∼16 min).

SFG and ATR-FTIR experiments

SFG involves a second order nonlinear optical process which requires two input beams. One input beam is a frequency fixed visible beam at 532 nm, and the other input beam is a frequency tunable IR beam (tuned from 1100 to 4300 cm^{-1}). The SFG signal can be generated when the two input beams overlap temporarily and spatially on the sample, which carries information of the second order nonlinear optical susceptibility $\chi^{(2)}$ of the sample. Due to the selection rule, $\chi^{(2)}$ is only non-zero when the medium has no inversion symmetry, such as surfaces and interfaces. Therefore, SFG is an intrinsic powerful tool for selectively probing surfaces and interfaces with sub-monolayer sensitivity. SFG has been widely applied to study both the conformation and orientation of interfacial proteins and peptides as previously reported.[27,30,31,33–36,38,42,48,49,51–56] Polarization measurements were used during SFG data collection. In this study, the near-total-reflection experimental setup was applied, as presented in previous publications.[27,51–56] Here ssp (s-polarized output SFG signal, s-polarized input visible beam, and p-polarized input IR beam) and ppp polarization combinations were used for SFG data collection of CYP2B4 or the CYP2B4–FBD protein complex associated with the lipid bilayer. The detected SFG intensity (I_{SFG}) can be expressed as[27–65]

$$I_{\mathrm{SFG}} \propto \left|\chi_{\mathrm{eff}}^{(2)}\right|^2 = \left|\chi_{\mathrm{NR}}^{(2)} + \sum_q \frac{A_q}{\omega_{\mathrm{IR}} - \omega_q + i\Gamma_q}\right|^2 \tag{1}$$

where $\chi_{\mathrm{eff}}^{(2)}$ is the effective second-order susceptibility. $\chi_{\mathrm{NR}}^{(2)}$ is contributed by the non-resonant background. A_q, ω_q, and Γ_q are the SFG signal amplitude, the vibrational frequency (peak center), and the damping coefficient (peak width) of the vibrational mode q, respectively. After obtaining these parameters from SFG spectral fitting, an SFG spectrum can then be constructed. In this study, the collected SFG spectra were fitted, and those fitting parameters were then used to reconstruct the SFG spectra without the contribution from the non-resonant background, in order to compare with the calculated SFG spectra from the Hamiltonian program discussed below where the non-resonant background contribution is also not considered. The SFG fitting parameters of various spectra presented in this article are listed in the SI, Section S1. The measured $\chi_{\mathrm{ppp}}^{(2)}/\chi_{\mathrm{ssp}}^{(2)}$ ratio can be obtained from the fitting parameters of SFG ssp and ppp spectra, and from which the $\chi_{\mathrm{zzz}}^{(2)}/\chi_{\mathrm{yyz}}^{(2)}$ ratio, defined in the lab coordination frame, can be deduced after considering the Fresnel coefficients.[83]

ATR-FTIR spectra were collected in the p and s polarizations. The detected ATR-FTIR intensity (I_{FTIR}) can be expressed as[80,81,83–87]

$$I_{\mathrm{FTIR}} = y + \sum_q A_q e^{-\left(\frac{x - x_q}{2w_q}\right)^2} \tag{2}$$

where y is an offset term, and A_q, x_q, and w_q are the ATR-FTIR signal amplitude, the vibrational frequency (peak center), and the peak width of the vibrational mode q, respectively. Similar to SFG, the collected ATR-FTIR spectra were reconstructed from the fitting parameters (offset term was omitted) and then the reconstructed ATR-FTIR spectra were used to compare with the calculated ATR-FTIR spectra as described below. The ATR-FTIR fitting parameters are listed in the SI, Section S1.

HADDOCK simulation

An online server of HADDOCK 2.4[88,89] was used to construct the structure of the CYP2B4–FBD protein complex. The initial individual structures used for CYP2B4 and FBD are obtained from the protein data bank with PDB ID of 3MVR and PDB ID of 1AMO (residues 64–235). The residues involved in the binding interface of CYP2B4 and FBD are listed in the SI Section S2.

Hamiltonian approach and scoring system

The details of the Hamiltonian approach spectral calculations were published previously[24,25,27,56,90] and will not be repeated here. For the SFG spectra calculations based on the structure of the protein complex from HADDOCK simulation, the local frequency of the amide unit was set to 1610 cm^{-1} for trunc-FBD and 1645 cm^{-1} for trunc-CYP2B4 with Γ_q of 10 cm^{-1}. For the ATR-FTIR spectra calculations, the local frequency of the amide unit was set to 1615 cm^{-1} for trunc-FBD and 1650 cm^{-1} for trunc-CYP2B4 with w_q of 20 cm^{-1}.

For the SFG spectra calculations based on the structure of trunc-CYP2B4 alone, the local frequency of the amide unit was set to 1650 cm^{-1} with Γ_q of 10 cm^{-1}. For the ATR-FTIR calculations, the local frequency of the amide unit was set to 1650 cm^{-1} with w_q of 20 cm^{-1}. The orientation dependent SFG spectra were calculated using the *z–x–z* convention rotation matrix.

All the reconstructed experimental SFG ssp (or ATR-FTIR s) spectra were normalized to [0, 1]. The SFG ppp (or ATR-FTIR p) spectra were scaled accordingly based on the maximum intensity ratio between SFG ppp and ssp spectra (or between ATR-FTIR p and s spectra). For Hamiltonian calculated spectra of the protein complex with isotope labeled trunc-FBD and trunc-CYP2B4 alone, the SFG ssp spectra (or ATR-FTIR s spectra) were also normalized to [0, 1], while the SFG ssp spectra (or ATR-FTIR s spectra) with the protein complex without isotope labeling on trunc-FBD and the protein complex without considering the coupling of the vibrational spectra of the two components in the complex, as well as all the calculated SFG ppp spectra (or trunc-FBA ATR- FTIR p spectra) were scaled accordingly. Then the calculated spectra were scored by comparing to the reconstructed experimental spectra in a point-by-point manner, as published previously.[24] The overall score of one structure under a certain orientation is the square root of the multiplication of the scores from both SFG and FTIR comparisons.

Definition of membrane orientation

Two vectors, $\mathbf{v}_1$ and $\mathbf{v}_2$, are defined as the vector from the center of mass (CoM) of the first 4 residues to the CoM of the last 4 residues of the I helix of trunc-CYP2B4, and the vector from the CoM of the first 4 residues of the C helix to the CoM of the last 4 residues of the F helix of the trunc-FBD, respectively. Angles α and β are defined as the angles of $\mathbf{v}_1$ and $\mathbf{v}_2$ *versus* the z axis (perpendicular to the membrane surface), respectively. θ_{heme} is defined as the angle between the heme plane (defined by the nitrogen atoms which are coordinated with iron) and the z axis. θ_{p} is defined as the angle between the α_1 helix in the trunc-FBD and the C helix in the trunc-CYP2B4.

Results and discussion

Data from SFG and ATR-FTIR measurements

Fig. 1(a) and (b) show the experimentally collected SFG amide I data of trunc-CYP2B4 associated with POPC and DLPC lipid bilayers, respectively. Fig. 1(c) displays the SFG spectra of the trunc-CYP2B4/trunc-FBD complex associated with the POPC lipid bilayer. The fitted results of these SFG spectra were listed in the SI, Section S1 and Tables S1–S3. With trunc-CYP2B4 alone associated with the POPC lipid membrane, a single peak at $\sim$1650 cm^{-1}, assigned to the α-helix structure, is predominant in each SFG ssp or ppp spectrum. When trunc-CYP2B4 was associated with a DLPC bilayer, besides the α-helical peak in the SFG ssp and ppp spectra, a small peak ($\sim$1635 cm^{-1}) of β-sheet was also observed in the SFG ppp spectrum. In addition, the peak widths of the SFG spectra of trunc-CYP2B4 with DLPC are narrower than the corresponding peak widths of trunc-CYP2B4 with POPC. These differences between SFG spectra indicated that the interfacial behavior of trunc-CYP2B4 may be influenced by the lipid compositions. After adding trunc-FBD to bind with trunc-CYP2B4, some low frequency peaks, *e.g.*, around 1610 cm^{-1}, were observed in both SFG ssp and ppp spectra collected from the protein complex (Fig. 1(c)). It is well known that ^{13}C labeled amide I group shifts its vibrational peak center by around 40 cm^{-1}, and therefore, the peaks at $\sim$1610 cm^{-1} can be assigned to the α-helix structures of isotope-labeled trunc-FBD. The peak around 1590 cm^{-1} in the SFG ppp spectrum, lower than the signal frequency of the isotope labeled α-helical structure, could be assigned to the parallel β-sheet structure of trunc-FBD. The predominant peak in each SFG spectrum shown in Fig. 1(c) is still centered at $\sim$1650 cm^{-1}, contributed by the α-helical structure of the unisotope-labeled trunc-CYP2B4. Trunc-CYP2B4 also contains some anti-parallel β-sheet structures, which could potentially contribute to the peak at $\sim$1630 cm^{-1}, overlapping with the trunc-FBD signals, at certain orientations. It is worth mentioning that although peaks from the β-sheet structures were not obviously seen from the SFG spectra of trunc-CYP2B4 alone, they could be more visible if trunc-CYP2B4 underwent orientation changes due to the binding with trunc-FBD, leading to the changes in SFG spectral features.

Fig. 2(a) and (b) show the experimentally collected ATR-FTIR amide I spectra of trunc-CYP2B4 associated with POPC and DLPC lipid bilayers, respectively. Fig. 2(c) presents the ATR-FTIR spectra of the trunc-CYP2B4/trunc-FBD complex associated with a POPC lipid bilayer. The fitted results of these ATR-FTIR spectra are listed in the SI, Section S1 and Tables S4–S6. Similar to SFG, isotope-labeled trunc-FBD contributed peaks at low frequencies ($\sim$1610 cm^{-1}) in both s and p ATR-FTIR spectra and unisotope-labeled trunc-CYP2B4 contributed peaks in high frequencies ($\sim$1645 to 1655 cm^{-1}). With different selection rules from SFG, FTIR can observe signals from random-coil structures of trunc-CYP2B4 centered at $\sim$1645 cm^{-1}.

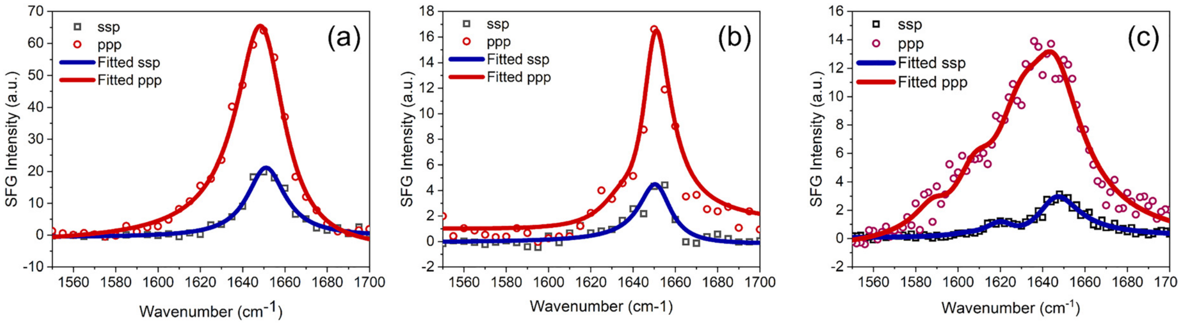

Fig. 1 Experimentally collected SFG ssp (black squares) and ppp (red circles) spectra of (a) trunc-CYP2B4 associated with a POPC lipid bilayer; (b) trunc-CYP2B4 associated with a DLPC lipid bilayer; and (c) trunc-FBD/trunc-CYP2B4 complex associated with a POPC bilayer. Solid lines are the fitted results.

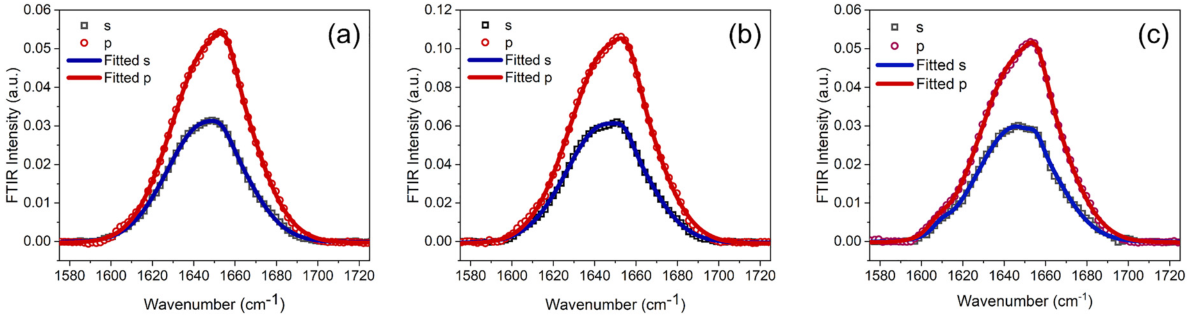

Fig. 2 Experimentally collected ATR-FTIR s (black squares) and p (red circles) spectra of (a) trunc-CYP2B4 associated with a POPC lipid bilayer; (b) trunc-CYP2B4 associated with a DLPC lipid bilayer; and (c) trunc-FBD/trunc-CYP2B4 complex associated with a POPC lipid bilayer. Solid lines are the fitted results.

Structure prediction *via* HADDOCK simulation

Crystal structures of trunc-CYP2B4 (PDB ID: 3MVR) and trunc-FBD (PDB ID: 1AMO, residues 64–235) are known, but the crystal structure of the complex is not available. Here, HADDOCK 2.4[88,89] was applied to derive possible structures of the trunc-CYP2B4/trunc-FBD complex. Crystal structures of trunc-CYP2B4 and trunc-FBD were used as input structures for the HADDOCK simulation, and the binding interface between two proteins was specified from previously reported data[1,22] (details shown in SI Section S2 and Table S7). HADDOCK starts with rigid body docking of two input proteins using the provided interfacial binding residues as ambiguous interaction restraints. The simulation was then followed by gradient driven energy minimization and molecular dynamics protocols to refine the residue side chains and the backbone at the binding interface of the protein complex. As a result, 85% of the output complex structures (170 out of 200 structures) were clustered into 11 groups based on structural similarity. The cluster occupied the best energy profile and the *Z*-score contains 18 similar complex structures (SI Section S2 and Table S8). These eighteen structures are very similar, as indicated by the mean RMSD listed in the SI, Table S8. These optimized complex structures (an example is shown in Fig. 3) show that the binding interface involves mostly basic residues of CYP2B4 (including R122, R126, R133, and K433) and acidic and hydrophobic residues of FBD (including N175, T177, and E179), in agreement with previous studies.[1,2] The edge to edge distance between heme and FMN is calculated to be 1.37 (±0.03) nm using GROMACS version 2022.2[91] (SI Section S2 and Table S9), which is around the predicted limit of 1.4 nm for electron transfer[92] and close to the FMN–heme distance of 1.8 nm determined using X-ray crystallography.[93] Previously, the conserved charged amino acid R125 of CYP2B4 was considered as a bridge between FMN and heme for electron transfer.[1] Here, the optimized output complex structures show that the side chain of this amino acid R125 is located between FMN and heme (Fig. 3), which is consistent with the previous findings.

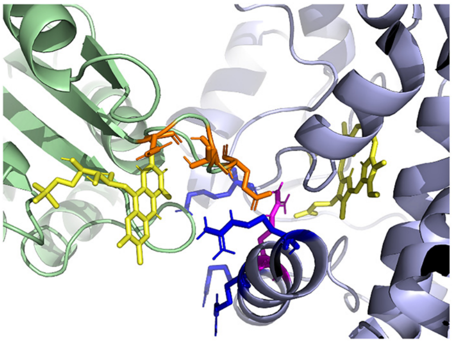

Fig. 3 Snapshot of one structure out of the 18 optimized output complex structures obtained from HADDOCK simulations. In the complex, trunc-FBD is in pale green and trunc-CYP2B4 is in light blue. Residues R122, R126, R133, and K433 of trunc-CYP2B4 are plotted with blue sticks, residues N175, T177, E179 of trunc-FBD are in orange sticks, the residue R125 of trunc-CYP2B4 is in magenta, and ligands are in yellow.

Hamiltonian spectra calculation of the trunc-CYP2B4/trunc-FBD complex associated with POPC lipid bilayer

The 18 energy-minimized structures obtained from HADDOCK simulations consider the interactions between the two components in the complex, but the membrane orientation of the complex and the most likely structure of the complex (among the 18 possible choices) are unknown. Here the 18 complex structures were directly input into the Hamiltonian program, and SFG ssp and ppp spectra and ATR-FTIR s and p spectra were calculated as a function of orientations (defined by the tilt angle θ and twist angle ψ) of the protein complex. The calculated SFG (or ATR-FTIR) spectra were compared to the reconstructed experimental SFG (or ATR-FTIR) spectra (reconstructed spectra were calculated using the spectral fitting parameters listed in the SI, Section S1 and Tables S1–S6) to search for the best matched orientation(s) and conformation(s) (among the 18 input structures). The highest ranked orientation of each structure was listed in the SI, Section S3. The highest score of each conformation falls in the range of [0.41, 0.45], with the lowest score (0.41) being only 9% lower than the highest score (0.45). This is reasonable because the 18 input structures are in the same cluster with similar conformations. The initial orientations (0°, 0°) of all the 18 input complex structures used for Hamiltonian spectral calculations have their principal axis aligned with the same direction but have different degrees of twist along this principal axis.

Among all the 18 input structures in the cluster with the lowest energy, the protein complex 11 (noted as PC11) at orientation of (80°, 210°) (or (100°, 30°)) possesses the highest matching score (= 0.45) with the experimental data. Thus, PC11 can be considered as the most likely conformation of the protein complex associated with the POPC bilayer with the most likely orientation of (80°, 210°) (or (100°, 30°)). It is worth noting that here in this study homodyne SFG measurements were conducted, therefore the orientation of (θ, ψ) and ($180° - \theta$, $\psi + 180°$) cannot be differentiated. Since PC11 has the highest matching score, and also shares similar conformation with the rest of the protein complex, it will be discussed as an example below.

Fig. 4(a) and 5(a) show the spectra matching qualities between the calculated spectra of PC11 at orientation (80°, 210°) (or (100°, 30°)) and the reconstructed experimental SFG and ATR-FTIR spectra (solid lines), respectively. The calculated and the reconstructed experimental spectra share similar spectral features and intensity ratios. In current Hamiltonian calculation, the local frequency of each amide unit within isotope-labeled trunc-FBD was set to ~1610 cm^{-1} (see details in the Methods section), which is different from that of the unisotope-labeled trunc-CYP2B4, which is at ~1645 cm^{-1}. To better understand the isotope-labeling effect, SFG and ATR-FTIR spectra of unisotope-labeled trunc-FBD/trunc-CYP2B4 complex PC11 were also calculated at the orientation (80°, 210°) (or (100°, 30°)). For this comparison calculation, the local frequency of trunc-FBD was set to 1645 cm^{-1}, the same as that of isotope-unlabeled CYP2B4 to exclude the isotope-labeling effect. The SFG spectra (Fig. 4(b) and (c)) (or ATR-FTIR spectra, shown in Fig. 5(b) and (c)) calculated with and without (blue dashed lines) isotope-labeling on trunc-FBD exhibit substantially different spectral features. Overall, without isotope-labeling on trunc-FBD, the low vibrational frequency peaks (1600–1630 cm^{-1}) were shifted back to the high frequency (~1650 cm^{-1}), and thus the intensity of the high frequency peaks became stronger. This trend was observed in all the SFG ssp and ppp spectra, and the ATR-FTIR s and p spectra, leading to more spectral overlaps. This change is more evident in the SFG spectra. Clearly, isotope-labeling one protein from a protein complex could shift the vibrational signals of the labeled protein to lower frequency to reduce the spectral overlaps, facilitating the spectral analysis of the protein complex.

To better understand the possible coupling effects of the vibrational spectra between two proteins in a protein complex, contributions from trunc-FBD and trunc-CYP2B4 in SFG and FTIR spectra were calculated by ignoring the off-diagonal coupling terms between the two proteins in the Hamiltonian

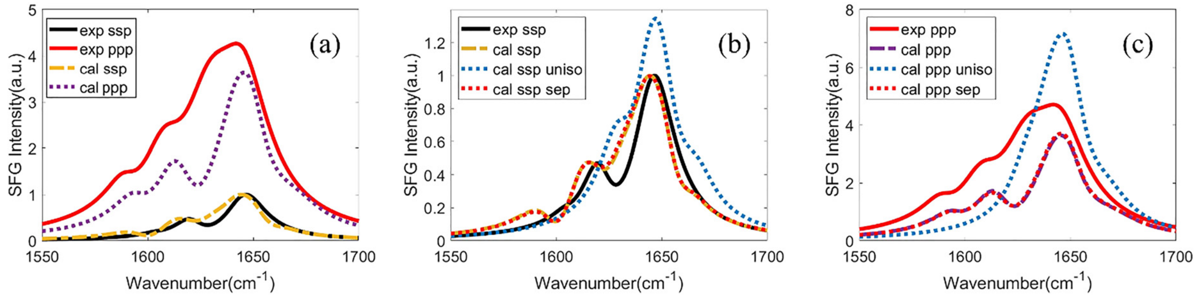

Fig. 4 (a) Comparison between reconstructed experimental (solid lines) and Hamiltonian approach calculated (dash lines) SFG ssp and ppp spectra; comparison between (b) SFG ssp spectrum and (c) SFG ppp spectrum of the reconstructed experimental spectra (solid line), calculated spectra from the protein complex using the Hamiltonian approach (yellow dashed line for ssp and purple dashed line for ppp spectra), calculated spectra with unisotope-labeling trunc-FBD in the protein complex (blue dashed lines), and calculated spectra without considering the off-diagonal coupling effects in Hamiltonian matrix (red dash lines). All spectra were calculated based on PC11 at the orientation of (80°, 210°) (or (100°, 30°)).

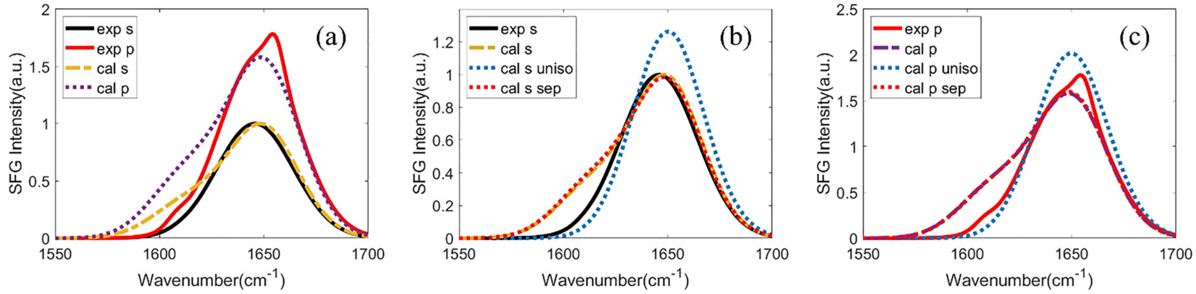

Fig. 5 (a) Comparison between reconstructed experimental (solid lines) and Hamiltonian calculated (dash lines) ATR-FTIR s and p spectra; comparison between (b) ATR-FTIR s spectrum and (c) ATR-FTIR p spectrum of reconstructed experimental spectra (solid line), calculated spectra from the protein complex with the Hamiltonian approach (yellow dashed line for s and purple dashed line for p spectra), calculated spectra using unisotope-labeling trunc-FBD in the protein complex (blue dashed lines), and calculated spectra without considering the off-diagonal coupling effects in Hamiltonian matrix (red dash lines). All spectra were calculated based on PC11 at the orientation of (80°, 210°) (or (100°, 30°)).

matrix using PC11 at orientation (80°, 210°) (or (100°, 30°)). The calculated SFG spectra (Fig. 4(b) and (c)) of the protein complex with (purple dashed line for SFG ppp spectrum and yellow dashed line for SFG ssp spectrum) and without (red dashed lines) considering the off-diagonal terms between the two proteins in the Hamiltonian matrix using PC11 show slight differences, but such differences are not significant. The enlarged spectra are shown in the SI, Fig. S1, for comparison. Similarly, the calculated ATR-FTIR spectra (Fig. 5(b) and (c)) of the protein complex with (purple dashed lines for ATR-FTIR p spectrum, yellow dashed line for ATR-FTIR s spectrum) and without (red dashed lines) considering the off-diagonal terms between the two proteins in the Hamiltonian matrix using PC11 also only show slight differences. This means that there is some off-diagonal coupling effect of the two proteins in the trunc-FBD/trunc-CYP2B4 complex, but such coupling effect is not substantial.

The PC11 structures associated with the POPC lipid bilayer at orientations (80°, 210°) and (100°, 30°) are shown in Fig. 6(a) and SI Section S5, Fig. S2(a). The orientation (80°, 210°) should be a more reasonable representation of the PC11 complex associated with the POPC lipid bilayer because here the FG helix containing the F′-G′ loop closely interacts with the lipid bilayer. The FG helix with the F′-G′ loop is widely accepted as a cell membrane interaction region when the TM domain is absent.[9,12,13] To simplify the further discussion, only the matched orientations that have the FG helix near the lipid bilayer will be discussed in details in the later sections. To better define the orientation of the structures that matched the experimental measurements *versus* the lipid membrane surface, and to compare our findings to the published results, additional orientation parameters, α, β, θ_{heme} and θ_{p}, were calculated for all the 18 structures at their matched orientations (only the orientations with the highest matching scores and with the FG helix near the lipid membrane surface were calculated; results are listed in the SI, Section S3 and Table S10). α and β are defined as the angles between the vector $\mathbf{v}_1$ and the z axis, and between the vector $\mathbf{v}_2$ and the z axis, respectively. The vector $\mathbf{v}_1$ aligns with the direction of the I helix of the trunc-CYP2B4 and $\mathbf{v}_2$ is in the direction from the C helix to the F helix of the trunc-CYP2B4. θ_{heme} is defined as the angle between the heme plane (determined by the nitrogen atoms coordinating with iron) and the z axis. θ_{p} is defined as the angle between the α_1 helix in the trunc-FBD and the C helix in the trunc-CYP2B4. Detailed definitions of these angles and vectors can be found in Fig. 6 and the Methods section. To differentiate these orientation parameters from those defined in the Hamiltonian program, we will refer (θ, ψ) defined in the Hamiltonian program as Hamiltonian orientation, and α, β, θ_{heme} and θ_{p} as the membrane orientation. The average angles calculated for all the 18 structures are: (i) α = 78° ± 3°; (ii) β = 116° ± 4°; (iii) θ_{heme} = 35° ± 5°; and (iv) θ_{p} = 103° ± 2°. Previously published studies showed that α is around 70°–83°, β is around 109°–127°, θ_{heme} is around 36°–59°, and θ_{p} is around 100° of a CYP/CPR complex.[9] Our results are well aligned with these published results.

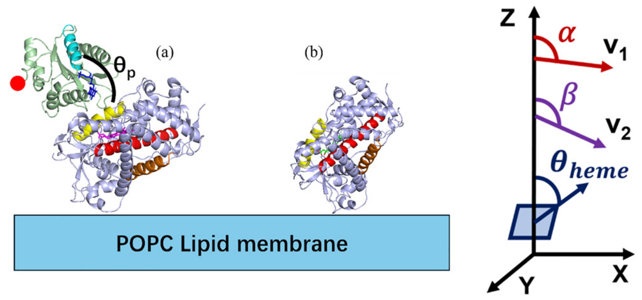

Fig. 6 (a) Most likely PC11 orientation: at Hamiltonian orientation of (80°, 210°); (b) most likely orientation of trunc-CYP2B4 from PC10: at Hamiltonian orientation of (30°, 330°). Trunc-FBD and trunc-CYP2B4 are in pale green and light blue, respectively. FMN is in blue and heme is in magenta. The α_1 helix of trunc-FBD (residues 91–105) is in cyan. N-terminus of trunc-FBD is in the red dot. I helix (residues 286–315), C helix (residues 119–134), and F helix (residues 192–210) of trunc-CYP2B4 are in red, yellow and orange, respectively. Vectors $\mathbf{v}_1$ and $\mathbf{v}_2$, and angles α, β, θ_{heme} and θ_{p} are defined in the Methods section.

Hamiltonian spectra calculation of the trunc-CYP2B4 associated with POPC and DLPC lipid bilayers

To understand the orientation difference of trunc-CYP2B4 before and after binding with trunc-FBD, the trunc-CYP2B4 structures with the best matched Hamiltonian orientations (only considering the orientations that have the FG helix near the lipid membrane surface) were extracted from the HADDOCK protein complexes. Such extracted trunc-CYP2B4 structures were used as new initial structures (set as (0°, 0°)) to calculate orientation dependent spectra using the Hamiltonian approach. Such spectra were compared to the reconstructed experimental spectra collected from the trunc-CYP2B4 associated with POPC and DLPC lipid bilayers without binding to trunc-FBD to determine the most likely structures of the trunc-CYP2B4 associated with the lipid bilayers alone. It was found that the trunc-CYP2B4 in complex structures PC101 and PC122 can have the highest matching scores for the POPC and DLPC cases respectively. The comparison results between the Hamiltonian approach calculated spectra and the reconstructed experimental SFG and ATR-FTIR spectra with the highest matching score are shown in Fig. 7. Further calculations of the deduced membrane orientations (results presented in the SI, Section S3 and Table S12) showed that, when the trunc-FBD is absent, α is 56 ± 3° in the case of POPC and 41 ± 4° in the case of DLPC. This indicates that originally trunc-CYP2B4 oriented the beginning of the I helix closer to the membrane with $\mathbf{v}_1$ tilting more away from (α is smaller) the membrane and transited to orient with the end of the I helix closer to the membrane with $\mathbf{v}_1$ pointing along with the membrane (α is bigger). Without the presence of the trunc-FBD, β is 96 ± 3° in trunc-CYP2B4 when associated with POPC and 74 ± 5° when associated with DLPC, which are smaller than the β (= 116 ± 4°) deduced in trunc-CYP2B4 after binding to the trunc-FBD. θ_{heme} is deduced to be 49° ± 3° in the case of POPC and 70° ± 4° in the case of DLPC of trunc-CYP2B4 alone, which are larger than the θ_{heme} (= 35° ± 5°) deduced from the trunc-CYP2B4/trunc-FBD complex. The changes of α and θ_{heme} indicated that trunc-CYP2B4 was tilting away/pulled up from the

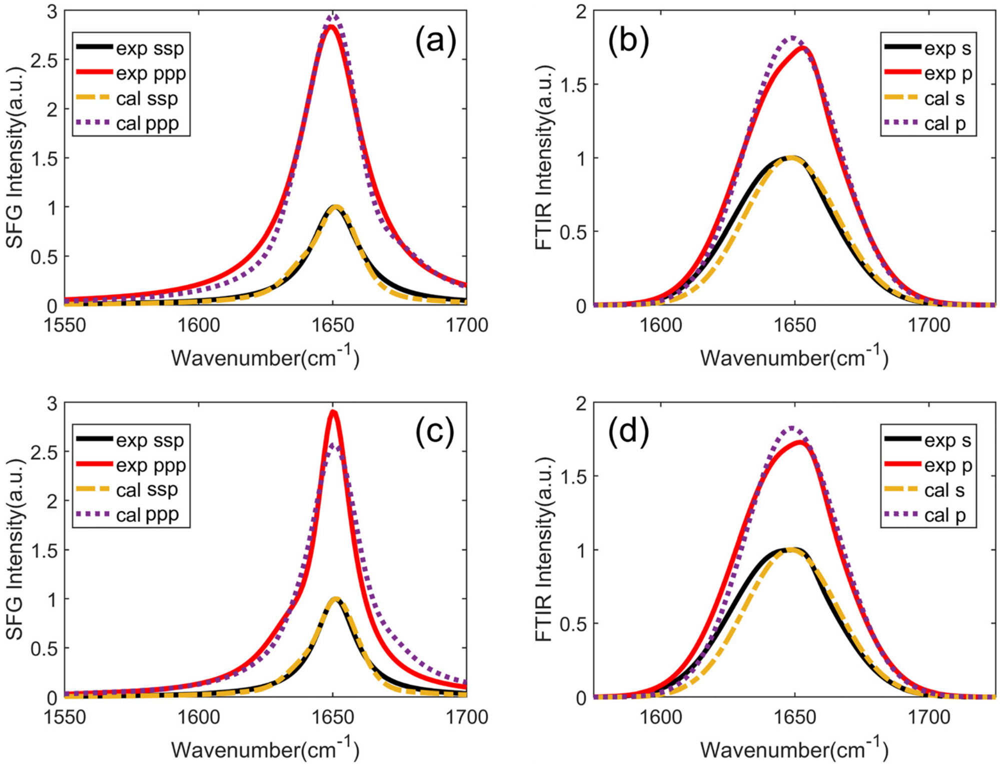

Fig. 7 Comparison between reconstructed experimental spectra and Hamiltonian calculated spectra of (a) SFG and (b) ATR-FTIR measurements based on the trunc-CYP2B4 of PC101 at the orientation (30°, 330°) or (150°, 150°) associated with a POPC lipid bilayer; and of (c) SFG and (d) ATR-FTIR measurements based on the trunc-CYP2B4 of PC122 at orientation (40°, 170°) or (140°, 350°) associated with a DLPC lipid bilayer.

membrane when binding with trunc-FBD and thus the lipid membrane/trunc-CYP2B4 interaction was weakened.

Conclusions

In this study, the conformations and orientations of the membrane-bound protein–protein complex composed of trunc-CYP2B4 and trunc-CYP2B4/trunc-FBD were successfully determined by the combined use of vibrational SFG and ATR-FTIR spectroscopies. Isotope labeling was introduced to distinguish trunc-FBD from trunc-CYP2B4 in spectra, enabling the separation of their respective signals. This technique allows for more accurate protein–protein complex structural studies by resolving signals from individual proteins within the complex.

It was found that upon binding *via* electrostatic interaction with trunc-FBD, trunc-CYP2B4 underwent a tilting motion, rotating away from the POPC membrane surface. This orientation change weakens its interaction with lipids, facilitating the accommodation of electrostatic interaction with trunc-FBD. Trunc-CYP2B4 was found to orient more towards the lipid membrane surface normal when associated with a DLPC lipid bilayer compared to a POPC lipid bilayer, indicating that the lipid composition likely influences the behavior of trunc-CYP2B4 to some extent in agreement with previous studies.[94–97] The obtained knowledge on the interfacial structures of membrane-bound trunc-CYP2B4 provides further understanding of its role in various cellular processes such as molecular recognition (of trunc-FBD) and electron transportation.

Understanding the interfacial structures (orientations and conformations) of membrane-bound proteins and protein complex is essential towards unraveling their functions related to signal transduction, disease mechanisms, drug development and biotechnological applications. The developed systematic methodology, combining the experimental measurements using non-invasive vibrational spectroscopies, structure simulations and Hamiltonian spectral calculations, can be a powerful tool to elucidate interfacial conformations and orientations of membrane-bound proteins *in situ*, facilitating our understanding of their biological functions and related applications.

Conflicts of interest

The authors declare no competing financial interest.

Data availability

The data supporting this article have been included in the main text and in the supplementary information (SI). Supplementary information: fitting parameters of SFG and ATR-FTIR measurements, parameters and results from the HADDOCK simulations, Hamiltonian spectral calculation and matching results, spectra comparison, and protein structure visualization. See DOI: https://doi.org/10.1039/d6cp00572a.

Acknowledgements

We thank the support from the University of Michigan. This study was partly supported by NIH (R35 GM139572 to A. R.). W. G. thanks the support from the Rackham predoctoral fellowship.

References

1 E. Prade, M. Mahajan, S. Im, M. Zhang, K. A. Gentry, G. M. Anantharamaiah, L. Waskell and A. Ramamoorthy, A Minimal Functional Complex of Cytochrome P450 and FBD of Cytochrome P450 Reductase in Nanodiscs, *Angew. Chem., Int. Ed.*, 2018, **57**(28), 8458–8462.

2 S.-C. Im and L. Waskell, The Interaction of Microsomal Cytochrome P450 2B4 with Its Redox Partners, Cytochrome P450 Reductase and Cytochrome B5, *Arch. Biochem. Biophys.*, 2011, **507**(1), 144–153.

3 M. Iijima, J. Ohnuki, T. Sato, M. Sugishima and M. Takano, Coupling of Redox and Structural States in Cytochrome P450 Reductase Studied by Molecular Dynamics Simulation, *Sci. Rep.*, 2019, **9**(1), 9341.

4 C. Chen, J. Min, L. Zhang, Y. Yang, X. Yu and R. Guo, Advanced Understanding of the Electron Transfer Pathway of Cytochrome P450s, *ChemBioChem*, 2021, **22**(8), 1317–1328.

5 A. V. Pandey and C. E. Flück, NADPH P450 Oxidoreductase: Structure, Function, and Pathology of Diseases, *Pharmacol. Ther.*, 2013, **138**(2), 229–254.

6 K. A. Gentry, M. Zhang, S.-C. Im, L. Waskell and A. Ramamoorthy, Substrate Mediated Redox Partner Selectivity of Cytochrome P450, *Chem. Commun.*, 2018, **54**(45), 5780–5783.

7 K. A. Gentry, G. M. Anantharamaiah and A. Ramamoorthy, Probing Protein–Protein and Protein–Substrate Interactions in the Dynamic Membrane-Associated Ternary Complex of Cytochromes P450, b_5, and Reductase, *Chem. Commun.*, 2019, **55**(89), 13422–13425.

8 W. R. Arnold, S. Zelasko, D. D. Meling, K. Sam and A. Das, Polymorphisms of CYP2C8 Alter First-Electron Transfer Kinetics and Increase Catalytic Uncoupling, *IJMS*, 2019, **20**(18), 4626.

9 G. Mukherjee, P. P. Nandekar and R. C. Wade, An Electron Transfer Competent Structural Ensemble of Membrane-Bound Cytochrome P450 1A1 and Cytochrome P450 Oxidoreductase, *Commun. Biol.*, 2021, **4**(1), 55.

10 M. Mahajan, T. Ravula, E. Prade, G. M. Anantharamaiah and A. Ramamoorthy, Probing Membrane Enhanced Protein–Protein Interactions in a Minimal Redox Complex of Cytochrome-P450 and P450-Reductase, *Chem. Commun.*, 2019, **55**(41), 5777–5780.

11 K. Berka, T. Hendrychová, P. Anzenbacher and M. Otyepka, Membrane Position of Ibuprofen Agrees with Suggested Access Path Entrance to Cytochrome P450 2C9 Active Site, *J. Phys. Chem. A*, 2011, **115**(41), 11248–11255.

12 C. Barnaba, B. R. Sahoo, T. Ravula, I. G. Medina-Meza, S.-C. Im, G. M. Anantharamaiah, L. Waskell and A. Ramamoorthy, Cytochrome-P450-Induced Ordering of Microsomal Membranes Modulates Affinity for Drugs, *Angew. Chem., Int. Ed.*, 2018, **57**(13), 3391–3395.

13 V. Cojocaru, K. Balali-Mood, M. S. P. Sansom and R. C. Wade, Structure and Dynamics of the Membrane-Bound Cytochrome P450 2C9, *PLoS Comput. Biol.*, 2011, **7**(8), e1002152.

14 Y. V. Grinkova, I. G. Denisov and S. G. Sligar, Functional Reconstitution of Monomeric CYP3A4 with Multiple Cytochrome P450 Reductase Molecules in Nanodiscs, *Biochem. Biophys. Res. Commun.*, 2010, **398**(2), 194–198.

15 U. H. N. Dürr, L. Waskell and A. Ramamoorthy, The Cytochromes P450 and B5 and Their Reductases–Promising Targets for Structural Studies by Advanced Solid-State NMR Spectroscopy, *Biochim. Biophys. Acta, Biomembr.*, 2007, **1768**(12), 3235–3259.

16 F. Li, P. F. Egea, A. J. Vecchio, I. Asial, M. Gupta, J. Paulino, R. Bajaj, M. S. Dickinson, S. Ferguson-Miller, B. C. Monk and R. M. Stroud, Highlighting Membrane Protein Structure and Function: A Celebration of the Protein Data Bank, *J. Biol. Chem.*, 2021, **296**, 100557.

17 J. C. Bozelli, S. S. Aulakh and R. M. Epand, Membrane Shape as Determinant of Protein Properties, *Biophys. Chem.*, 2021, **273**, 106587.

18 F. Orädd and M. Andersson, Tracking Membrane Protein Dynamics in Real Time, *J. Membr. Biol.*, 2021, **254**(1), 51–64.

19 S. A. Ghadami, K. Ahadi-Amandi, R. Khodarahmi, S. Ghanbari and H. Adibi, Synthesis of Benzylidene-Indandione Derivatives as Quantification of Amyloid Fibrils, *Biophys. Chem.*, 2023, **296**, 106982.

20 L. Paço, J. C. Hackett and W. M. Atkins, Nanodisc-Embedded Cytochrome P450 P3A4 Binds Diverse Ligands by Distributing Conformational Dynamics to Its Flexible Elements, *J. Inorg. Biochem.*, 2023, **244**, 112211.

21 A. Bridges, L. Gruenke, Y.-T. Chang, I. A. Vakser, G. Loew and L. Waskell, Identification of the Binding Site on Cytochrome P450 2B4 for Cytochrome b 5 and Cytochrome P450 Reductase, *J. Biol. Chem.*, 1998, **273**(27), 17036–17049.

22 M. Wang, D. L. Roberts, R. Paschke, T. M. Shea, B. S. S. Masters and J.-J. P. Kim, Three-Dimensional Structure of NADPH–Cytochrome P450 Reductase: Prototype for FMN- and FAD-Containing Enzymes, *Proc. Natl. Acad. Sci. U. S. A.*, 1997, **94**(16), 8411–8416.

23 B. Krishnarjuna, S.-C. Im, T. Ravula, J. Marte, R. J. Auchus and A. Ramamoorthy, Non-Ionic Inulin-Based Polymer Nanodiscs Enable Functional Reconstitution of a Redox Complex Composed of Oppositely Charged CYP450 and CPR in a Lipid Bilayer Membrane, *Anal. Chem.*, 2022, **94**(34), 11908–11915.

24 W. Guo, X. Zou, H. Jiang, K. J. Koebke, M. Hoarau, R. Crisci, T. Lu, T. Wei, E. N. G. Marsh and Z. Chen, Molecular

Structure of the Surface-Immobilized Super Uranyl Binding Protein, *J. Phys. Chem. B*, 2021, **125**(28), 7706–7716.

25 T. Lu, W. Guo and Z. Chen, Probing Protein Aggregation at Buried Interfaces: Distinguishing Adsorbed Protein Monomer, Dimer, and Monomer-Dimer Mixture in Situ, *Chem. Sci.*, 2022, **13**(4), 975–984.

26 P. Yang, A. Ramamoorthy and Z. Chen, Membrane Orientation of MSI-78 Measured by Sum Frequency Generation Vibrational Spectroscopy, *Langmuir*, 2011, **27**(12), 7760–7767.

27 W. Guo, T. Lu, R. Crisci, S. Nagao, T. Wei and Z. Chen, Determination of Protein Conformation and Orientation at Buried Solid/Liquid Interfaces, *Chem. Sci.*, 2023, **14**(11), 2999–3009.

28 W. Sung, D. Kim and Y. R. Shen, Sum-Frequency Vibrational Spectroscopic Studies of Langmuir Monolayers, *Curr. Appl. Phys.*, 2013, **13**(4), 619–632.

29 K. B. Eisenthal, Liquid Interfaces Probed by Second-Harmonic and Sum-Frequency Spectroscopy, *Chem. Rev.*, 1996, **96**(4), 1343–1360.

30 K. Strunge, N. Hoinkis, H. Lutz, S. Alamdari, S. J. Roeters, H. Lu, J. Pfaendtner and T. Weidner, Peptide Mimic of the Marine Sponge Protein Silicatein Fabricates Ultrathin Nanosheets of Silicon Dioxide and Titanium Dioxide, *Langmuir*, 2022, **38**(26), 8087–8093.

31 S. Alamdari, S. J. Roeters, T. W. Golbek, L. Schmüser, T. Weidner and J. Pfaendtner, Orientation and Conformation of Proteins at the Air–Water Interface Determined from Integrative Molecular Dynamics Simulations and Sum Frequency Generation Spectroscopy, *Langmuir*, 2020, **36**(40), 11855–11865.

32 T. W. Golbek, L. Schmüser, M. H. Rasmussen, T. B. Poulsen and T. Weidner, Lasalocid Acid Antibiotic at a Membrane Surface Probed by Sum Frequency Generation Spectroscopy, *Langmuir*, 2020, **36**(12), 3184–3192.

33 S. Hosseinpour, S. J. Roeters, M. Bonn, W. Peukert, S. Woutersen and T. Weidner, Structure and Dynamics of Interfacial Peptides and Proteins from Vibrational Sum-Frequency Generation Spectroscopy, *Chem. Rev.*, 2020, **120**(7), 3420–3465.

34 J. Tan, B. Zhang, Y. Luo and S. Ye, Ultrafast Vibrational Dynamics of Membrane-Bound Peptides at the Lipid Bilayer/Water Interface, *Angew. Chem., Int. Ed.*, 2017, **56**(42), 12977–12981.

35 J. Huang, K. Tian, S. Ye and Y. Luo, Amide III SFG Signals as a Sensitive Probe of Protein Folding at Cell Membrane Surface, *J. Phys. Chem. C*, 2016, **120**(28), 15322–15328.

36 S. Roy, P. A. Covert, W. R. FitzGerald and D. K. Hore, Biomolecular Structure at Solid–Liquid Interfaces As Revealed by Nonlinear Optical Spectroscopy, *Chem. Rev.*, 2014, **114**(17), 8388–8415.

37 C. Zhang, J. N. Myers and Z. Chen, Molecular Behavior at Buried Epoxy/Poly(ethylene terephthalate) Interface, *Langmuir*, 2014, **30**, 12541–12550.

38 L. Fu, J. Liu and E. C. Y. Yan, Chiral Sum Frequency Generation Spectroscopy for Characterizing Protein Secondary Structures at Interfaces, *J. Am. Chem. Soc.*, 2011, **133**(21), 8094–8097.

39 P. Chen, S. Westerberg, K. Y. Kung, J. Zhu, J. Grunes and G. A. Somorjai, CO Poisoning of Catalytic Ethylene Hydrogenation on the Pt (111) Surface Studied by Surface Sum Frequency Generation, *Appl. Catal., A*, 2002, **229**(1–2), 147–154.

40 P. Chen, K. Y. Kung, Y. R. Shen and G. A. Somorjai, Sum Frequency Generation Spectroscopic Study of CO/Ethylene Coadsorption on the Pt (111) Surface and CO Poisoning of Catalytic Ethylene Hydrogenation, *Surf. Sci.*, 2001, **494**(3), 289–297.

41 T. Jarisz, S. Roy and D. K. Hore, Surface Water as a Mediator and Reporter of Adhesion at Aqueous Interfaces, *Acc. Chem. Res.*, 2018, **51**(9), 2287–2295.

42 S. Wang, W. Sun, S. Guo, X. Liu and X. Han, Effects of Chiral Molecule Modification on Surface Biosorption Behavior, *Langmuir*, 2021, **37**(15), 4441–4448.

43 K. D. Judd, N. M. Gonzalez, T. Yang and P. S. Cremer, Contact Ion Pair Formation Is Not Necessarily Stronger than Solvent Shared Ion Pairing, *J. Phys. Chem. Lett.*, 2022, **13**(3), 923–930.

44 N. W. Ulrich, J. Andra, J. Williamson, K.-W. Lee and Z. Chen, Plasma Treatment Effect on Polymer Buried interfacial Structure and Property, *Phys. Chem. Chem. Phys.*, 2017, **19**, 12144–12155.

45 Y. Li, T. L. Ogorzalek, S. Wei, X. Zhang, P. Yang, J. Jasensky, C. L. Brooks, E. N. G. Marsh and Z. Chen, Effect of Immobilization Site on the Orientation and Activity of Surface-Tethered Enzymes, *Phys. Chem. Chem. Phys.*, 2018, **20**, 1021–1029.

46 C. Zhang, J. Meyers and Z. Chen, Elucidation of Molecular Structures at Buried Polymer Interfaces and Biological Interfaces Using Sum Frequency Generation Vibrational Spectroscopy, *Soft Matter*, 2013, **9**, 4738–4761.

47 J. Tan, Q. Pei, L. Zhang and S. Ye, Evidence for a Local Field Effect in Surface Plasmon-Enhanced Sum Frequency Generation Vibrational Spectra, *Langmuir*, 2022, **38**(19), 6099–6105.

48 J. Tan, J. Zhang, Y. Luo and S. Ye, Misfolding of a Human Islet Amyloid Polypeptide at the Lipid Membrane Populates through β-Sheet Conformers without Involving α-Helical Intermediates, *J. Am. Chem. Soc.*, 2019, **141**(5), 1941–1948.

49 S. Ye, H. Li, W. Yang and Y. Luo, Accurate Determination of Interfacial Protein Secondary Structure by Combining Interfacial-Sensitive Amide I and Amide III Spectral Signals, *J. Am. Chem. Soc.*, 2014, **136**(4), 1206–1209.

50 X. Hu, J. Tan and S. Ye, Reversible Activation of PH-Responsive Cell-Penetrating Peptides in Model Cell Membrane Relies on the Nature of Lipid, *J. Phys. Chem. C*, 2017, **121**(28), 15181–15187.

51 X. Han, Y. Liu, F.-G. Wu, J. Jansensky, T. Kim, Z. Wang, C. L. Brooks, J. Wu, C. Xi, C. M. Mello and Z. Chen, Different Interfacial Behaviors of Peptides Chemically Immobilized on Surfaces with Different Linker Lengths and via Different Termini, *J. Phys. Chem. B*, 2014, **118**(11), 2904–2912.

52 X. Han, L. Soblosky, M. Slutsky, C. M. Mello and Z. Chen, Solvent Effect and Time-Dependent Behavior of C-Terminus-Cysteine-Modified Cecropin P1 Chemically Immobilized on a Polymer Surface, *Langmuir*, 2011, **27**(11), 7042–7051.

53 X. Han, J. Zheng, F. Lin, K. Kuroda and Z. Chen, Interactions between Surface-Immobilized Antimicrobial Peptides and Model Bacterial Cell Membranes, *Langmuir*, 2018, **34**(1), 512–520.

54 X. Chen, J. Wang, J. J. Sniadecki, M. A. Even and Z. Chen, Probing α-Helical and β-Sheet Structures of Peptides at Solid/Liquid Interfaces with SFG, *Langmuir*, 2005, **21**(7), 2662–2664.

55 B. Ding, L. Soblosky, K. Nguyen, J. Geng, X. Yu, A. Ramamoorthy and Z. Chen, Physiologically-Relevant Modes of Membrane Interactions by the Human Antimicrobial Peptide, LL-37, Revealed by SFG Experiments, *Sci. Rep.*, 2013, **3**(1), 1854.

56 B. Ding, A. Panahi, J.-J. Ho, J. E. Laaser, C. L. I. Brooks, M. T. Zanni and Z. Chen, Probing Site-Specific Structural Information of Peptides at Model Membrane Interface In Situ, *J. Am. Chem. Soc.*, 2015, **137**(32), 10190–10198.

57 J. S. Andre, N. Escoffery, N. W. Ulrich, Y. Wu, W. Guo, M. Yang, J. Myers and Z. Chen, Ultraviolet Light-Sensitive Debonding Layer for Reducing Adhesion of Polymer Adhesives for Recycling, *J. Phys. Chem. C*, 2022, **126**(44), 18907–18917.

58 A. Chandra and A. Chandra, Effects of Salt Concentration on the Structure and Vibrational Sum Frequency Generation Spectra of Liquid/Vapor Interfaces of Aqueous Solutions of Metal Nitrates, *Phys. Chem. Chem. Phys.*, 2025, **27**(37), 19748–19761.

59 M. Zelenka and E. H. G. Backus, MgO-water Interface: Structure and Surface Dissolution Depend on Flow and pH, *Phys. Chem. Chem. Phys.*, 2025, **27**(43), 23356–23364.

60 L. Bromley, P. E. Videla, J. L. Cartagena-Brigantty, V. S. Batista and L. Velarde, Binding and Orientation of Carbamate Pesticides on Silica Surfaces, *J. Phys. Chem. C*, 2023, **127**(17), 8399–8410.

61 Y. Nojima, T. Shimoaka, T. Hasegawa and T. Ishibashi, Molecular Orientations of Myristic Acid Derivatives with Different Perfluoroalkyl Chain Lengths at the Air/Water Interface Evaluated by Heterodyne-Detected Sum Frequency Generation Spectroscopy, *J. Phys. Chem. C*, 2023, **127**(25), 12349–12356.

62 O. Kroutil, S. Pezzotti, M.-P. Gaigeot and M. Předota, Phase-Sensitive Vibrational SFG Spectra from Simple Classical Force Field Molecular Dynamics Simulations, *J. Phys. Chem. C*, 2020, **124**(28), 15253–15263.

63 C. Du, R. S. Andino, M. C. Rotondaro, S. W. Devlin, S. Erramilli, L. D. Ziegler and M. M. Thuo, Substrate Roughness and Tilt Angle Dependence of Sum-Frequency Generation Odd–Even Effects in Self-Assembled Monolayers, *J. Phys. Chem. C*, 2022, **126**(16), 7294–7306.

64 D. Zhou, A. Ge, T. Kogina, K. Inoue, Y.-X. Chen and S. Ye, Molecular Structures at Nafion/Graphene Interfaces Investigated by Sum-Frequency Generation Spectroscopy, *J. Phys. Chem. C*, 2022, **126**(14), 6523–6530.

65 F. M. Geiger and G. V. Hartland, Sixty Years of Surface-Specific Spectroscopy, *J. Phys. Chem. C*, 2022, **126**(34), 14375–14379.

66 P. Hamm and M. Zanni, *Concepts and Methods of 2D Infrared Spectroscopy*, Cambridge University Press, Cambridge, UK, 2011.

67 A. M. Woys, Y.-S. Lin, A. S. Reddy, W. Xiong, J. J. de Pablo, J. L. Skinner and M. T. Zanni, 2D IR Line Shapes Probe Ovispirin Peptide Conformation and Depth in Lipid Bilayers, *J. Am. Chem. Soc.*, 2010, **132**(8), 2832–2838.

68 M. J. Ryan, L. Gao, F. I. Valiyaveetil, M. T. Zanni and A. A. Kananenka, Probing Ion Configurations in the KcsA Selectivity Filter with Single-Isotope Labels and 2D IR Spectroscopy, *J. Am. Chem. Soc.*, 2023, **145**(33), 18529–18537.

69 M. Maj, J. P. Lomont, K. L. Rich, A. M. Alperstein and M. T. Zanni, Site-Specific Detection of Protein Secondary Structure Using 2D IR Dihedral Indexing: A Proposed Assembly Mechanism of Oligomeric HIAPP, *Chem. Sci.*, 2018, **9**(2), 463–474.

70 S. Paul, A. Jeništová, F. Vosough, E. Berntsson, C. Mörman, J. Jarvet, A. Gräslund, S. K. T. S. Wärmländer and A. Barth, ^{13}C- and ^{15}N-Labeling of Amyloid-β and Inhibitory Peptides to Study Their Interaction via Nanoscale Infrared Spectroscopy, *Commun. Chem.*, 2023, **6**(1), 163.

71 H. Maekawa, G. Ballano, F. Formaggio, C. Toniolo and N.-H. Ge, The 13C = 18O/15N Isotope Dependence of the Amide-I/II 2D IR Cross Peaks for the Fully-Extended Peptides, *J. Phys. Chem. B*, 2014, **118**(50), 29448–29457.

72 S. D. Moran, S. M. Decatur and M. T. Zanni, Structural and Sequence Analysis of the Human γD-Crystallin Amyloid Fibril Core Using 2D IR Spectroscopy, Segmental ^{13}C Labeling, and Mass Spectrometry, *J. Am. Chem. Soc.*, 2012, **134**(44), 18410–18416.

73 A. S. Saribas, L. Gruenke and L. Waskell, Overexpression and Purification of the Membrane-Bound Cytochrome P450 2B4, *Protein Expr. Purif.*, 2001, **21**(2), 303–309.

74 M. Zhang, R. Huang, S.-C. Im, L. Waskell and A. Ramamoorthy, Effects of Membrane Mimetics on Cytochrome P450-Cytochrome B5 Interactions Characterized by NMR Spectroscopy, *J. Biol. Chem.*, 2015, **290**(20), 12705–12718.

75 R. Huang, M. Zhang, F. Rwere, L. Waskell and A. Ramamoorthy, Kinetic and Structural Characterization of the Interaction between the FMN Binding Domain of Cytochrome P450 Reductase and Cytochrome *c*, *J. Biol. Chem.*, 2015, **290**(8), 4843–4855.

76 S. Ye, H. Li, F. Wei, J. Jasensky, A. P. Boughton, P. Yang and Z. Chen, Observing a Model Ion Channel Gating Action in Model Cell Membranes in Real Time in Situ: Membrane Potential Change Induced Alamethicin Orientation Change, *J. Am. Chem. Soc.*, 2012, **134**(14), 6237–6243.

77 P. Yang, F.-G. Wu and Z. Chen, Dependence of Alamethicin Membrane Orientation on the Solution Concentration, *J. Phys. Chem. C*, 2013, **117**(7), 3358–3365.

78 P. Yang, F.-G. Wu and Z. Chen, Lipid Fluid-Gel Phase Transition Induced Alamethicin Orientational Change

Probed by Sum Frequency Generation Vibrational Spectroscopy, *J. Phys. Chem. C*, 2013, **117**(33), 17039–17049.

79 A. P. Boughton, P. Yang, V. M. Tesmer, B. Ding, J. J. G. Tesmer and Z. Chen, Heterotrimeric G Protein $\beta_1\gamma_2$ Subunits Change Orientation upon Complex Formation with G Protein-Coupled Receptor Kinase 2 (GRK2) on a Model Membrane, *Proc. Natl. Acad. Sci. U. S. A.*, 2011, **108**(37), 15019.

80 P. Yang, A. Boughton, K. T. Homan, J. J. G. Tesmer and Z. Chen, Membrane Orientation of Gαiβ1γ2 and Gβ1γ2 Determined via Combined Vibrational Spectroscopic Studies, *J. Am. Chem. Soc.*, 2013, **135**(13), 5044–5051.

81 P. Yang, A. Glukhova, J. J. G. Tesmer and Z. Chen, Membrane Orientation and Binding Determinants of G Protein-Coupled Receptor Kinase 5 as Assessed by Combined Vibrational Spectroscopic Studies, *PLoS One*, 2013, **8**(11), e82072.

82 E. Kalb, S. Frey and L. K. Tamm, Formation of Supported Planar Bilayers by Fusion of Vesicles to Supported Phospholipid Monolayers, *Biochim. Biophys. Acta, Biomembr.*, 1992, **1103**(2), 307–316.

83 X. Zou, S. Wei, J. Jasensky, M. Xiao, Q. Wang, C. L. Brooks and Z. Chen, Molecular Interactions between Graphene and Biological Molecules, *J. Am. Chem. Soc.*, 2017, **139**(5), 1928–1936.

84 Y. Liu, T. L. Ogorzalek, P. Yang, M. M. Schroeder, E. N. G. Marsh and Z. Chen, Molecular Orientation of Enzymes Attached to Surfaces through Defined Chemical Linkages at the Solid–Liquid Interface, *J. Am. Chem. Soc.*, 2013, **135**(34), 12660–12669.

85 L. Shen, M. Schroeder, T. L. Ogorzalek, P. Yang, F.-G. Wu, E. N. G. Marsh and Z. Chen, Surface Orientation Control of Site-Specifically Immobilized Nitro-Reductase (NfsB), *Langmuir*, 2014, **30**(20), 5930–5938.

86 X. Zou, S. Wei, S. Badieyan, M. Schroeder, J. Jasensky, C. L. Brooks, E. N. G. Marsh and Z. Chen, Investigating the Effect of Two-Point Surface Attachment on Enzyme Stability and Activity, *J. Am. Chem. Soc.*, 2018, **140**(48), 16560–16569.

87 P. Yu, Synchrotron IR Microspectroscopy for Protein Structure Analysis: Potential and Questions, *Spectroscopy*, 2006, **20**(5,6), 229–251.

88 R. V. Honorato, P. I. Koukos, B. Jiménez-García, A. Tsaregorodtsev, M. Verlato, A. Giachetti, A. Rosato and A. M. J. J. Bonvin, Structural Biology in the Clouds: The WeNMR-EOSC Ecosystem, *Front. Mol. Biosci.*, 2021, **8**, 729513.

89 G. C. P. van Zundert, J. P. G. L. M. Rodrigues, M. Trellet, C. Schmitz, P. L. Kastritis, E. Karaca, A. S. J. Melquiond, M. van Dijk, S. J. de Vries and A. M. J. J. Bonvin, The HADDOCK2.2 Web Server: User-Friendly Integrative Modeling of Biomolecular Complexes, *J. Mol. Biol.*, 2016, **428**(4), 720–725.

90 T. Lu and Z. Chen, Monitoring the Molecular Structure of Fibrinogen during the Adsorption Process at the Buried Silicone Oil Interface In Situ in Real Time, *J. Phys. Chem. Lett.*, 2023, **14**(13), 3139–3145.

91 M. J. Abraham, T. Murtola, R. Schulz, S. Páll, J. C. Smith, B. Hess and E. Lindahl, GROMACS: High Performance Molecular Simulations through Multi-Level Parallelism from Laptops to Supercomputers, *SoftwareX*, 2015, **1–2**, 19–25.

92 C. Page, Mechanism for Electron Transfer within and between Proteins, *Curr. Opin. Chem. Biol.*, 2003, **7**(5), 551–556.

93 I. F. Sevrioukova, H. Li, H. Zhang, J. A. Peterson and T. L. Poulos, Structure of a Cytochrome P450–Redox Partner Electron-Transfer Complex, *Proc. Natl. Acad. Sci. U. S. A.*, 1999, **96**(5), 1863–1868.

94 C. Barnaba, T. Ravula, I. G. Medina-Meza, S.-C. Im, G. M. Anantharamaiah, L. Waskell and A. Ramamoorthy, Lipid-Exchange in Nanodiscs Discloses Membrane Boundaries of Cytochrome-P450 Reductase, *Chem. Commun.*, 2018, **54**(49), 6336–6339.

95 A. Das and S. G. Sligar, Modulation of the Cytochrome P450 Reductase Redox Potential by the Phospholipid Bilayer, *Biochemistry*, 2009, **48**(51), 12104–12112.

96 T. Ravula, C. Barnaba, M. Mahajan, G. M. Anantharamaiah, S.-C. Im, L. Waskell and A. Ramamoorthy, Membrane Environment Drives Cytochrome P450's Spin Transition and Its Interaction with Cytochrome b_5, *Chem. Commun.*, 2017, **53**(95), 12798–12801.

97 Lipid-Protein Interactions: Methods and Protocols, ed. Kleinschmidt, J. H., *Methods in Molecular Biology*, Springer, New York, NY, 2019, vol. 2003.